Journal of Structural Biology 213 (2021) 107724

Contents lists available at ScienceDirect

Journal of Structural Biology

journal homepage: www.elsevier.com/locate/yjsbi

Small-angle neutron scattering solution structures of NADPH-dependent sulfite reductase

Daniel T. Murray [a], Kevin L. Weiss [b], Christopher B. Stanley [b,c], Gergely Nagy [b], M. Elizabeth Stroupe [a,*]

[a] Department of Biological Science and Institute of Molecular Biophysics, Florida State University, Tallahassee, FL 32306, USA
[b] Neutron Scattering Division, Oak Ridge National Laboratory, Oak Ridge, TN 37830, USA
[c] Computational Sciences and Engineering Division, Oak Ridge National Laboratory, Oak Ridge, TN 37830, USA

ARTICLE INFO

Keywords:
Analytical ultracentrifugation
Assimilatory NADPH-dependent sulfite reductase
Electron transfer
Oxidoreductase
Solution scattering

ABSTRACT

Sulfite reductase (SiR), a dodecameric complex of flavoprotein reductase subunits (SiRFP) and hemoprotein oxidase subunits (SiRHP), reduces sulfur for biomass incorporation. Electron transfer within SiR requires intra- and inter-subunit interactions that are mediated by the relative position of each protein, governed by flexible domain movements. Using small-angle neutron scattering, we report the first solution structures of SiR heterodimers containing a single copy of each subunit. These structures show how the subunits bind and how both subunit binding and oxidation state impact SiRFP's conformation. Neutron contrast matching experiments on selectively deuterated heterodimers allow us to define the contribution of each subunit to the solution scattering. SiRHP binding induces a change in the position of SiRFP's flavodoxin-like domain relative to its ferredoxin-$NADP^+$ reductase domain while compacting SiRHP's N-terminus. Reduction of SiRFP leads to a more open structure relative to its oxidized state, re-positioning SiRFP's N-terminal flavodoxin-like domain towards the SiRHP binding position. These structures show, for the first time, how both SiRHP binding to, and reduction of, SiRFP positions SiRFP for electron transfer between the subunits.

1. Introduction

Multi-subunit oxidoreductase enzymes catalyze electron transfer reduction–oxidation (redox) reactions that drive energy flux in cells. A conserved class of NADPH-dependent diflavin reductases funnel electrons from NADPH through flavin adenine dinucleotide (FAD) and flavin mononucleotide (FMN) cofactors to diverse oxidases that are often metalloenzymes. Assimilatory NADPH-dependent sulfite reductase (SiR) is a member of this class of enzymes and is responsible for the six-electron reduction of sulfite (SO_3^{2-}) to sulfide (S^{2-}) for incorporation into sulfur-containing biomolecules (Siegel et al., 1973). These SiRs are dodecameric, with a uniquely octameric diflavin reductase (SiRFP, the α subunit, Fig. 1a) and four copies of a siroheme- and Fe_4S_4-containing hemoprotein (SiRHP, the β subunit, Fig. 1b) (Murphy et al., 1973; Siegel and Davis, 1974; Siegel et al., 1974).

SiR's $\alpha_8\beta_4$ dodecameric assembly sets it apart from other members of this class of diflavin reductase-dependent enzymes like cytochrome P450 reductase (CPR), nitric oxide synthase (NOS), cytochrome P102, and methionine synthase (Campbell et al., 2014; Olteanu and Banerjee, 2001; Xia et al., 2011a; Zhang et al., 2018). Based on what is known about the well-studied CPR (Freeman et al., 2017, 2018), electron transfer within the SiR diflavin reductase subunit is hypothesized to work through a redox-sensitive conformational change between two domains that are separated by a flexible hinge. Specifically, the FMN-binding domain, which is homologous to small flavodoxins (Fld), moves close to the NADPH-reduced FAD, which binds to a ferredoxin-$NADP^+$ reductase (FNR) domain, to itself become reduced (Huang et al., 2013; Iyanagi et al., 2012; Wang et al., 1997). Upon $NADP^+$ release, the Fld domain swivels back out to pass the electrons to its oxidase partner (Hamdane et al., 2009; Xia et al., 2011b). In CPR, the opening of the Fld domain creates the binding site for the heme-containing oxidase (Im and Waskell, 2011). In NOS, where the two subunits are expressed in a single

Abbreviations: SiR, assimilatory NADPH-dependent sulfite reductase; SiRFP, sulfite reductase flavoprotein; SiRHP, sulfite reductase hemoprotein; D-SiRHP, partially deuterated SiRHP; Fld, flavodoxin-like domain; FNR, ferredoxin-$NADP^+$ reductase domain; SANS, small-angle neutron scattering; CMP, contrast match point; AUC, analytical ultracentrifugation.

* Corresponding author at: 91 Chieftan Way, Tallahassee, FL 32306, USA.
E-mail address: mestroupe@bio.fsu.edu (M.E. Stroupe).

https://doi.org/10.1016/j.jsb.2021.107724
Received 6 January 2021; Received in revised form 4 March 2021; Accepted 8 March 2021
Available online 13 March 2021

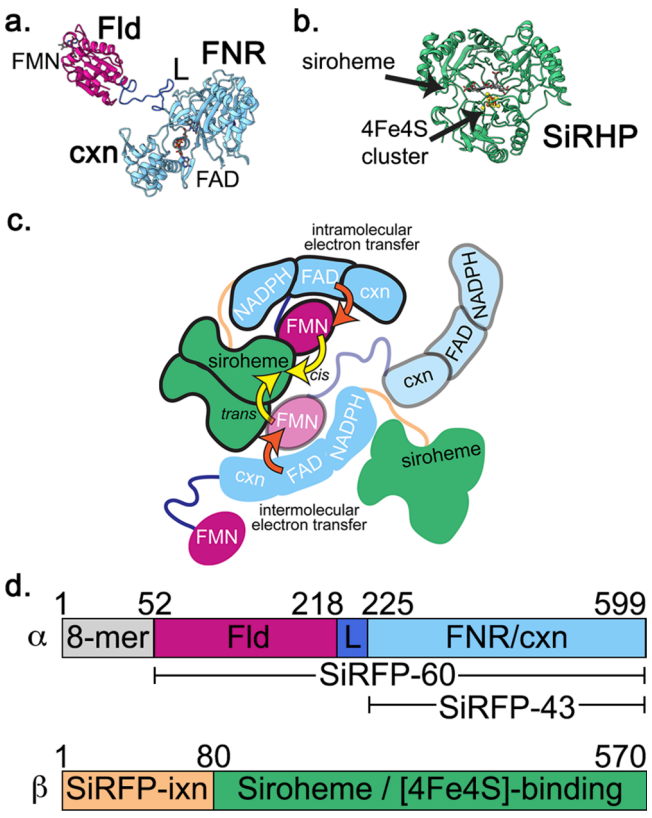

Fig. 1. SiR domain composition and structure. **a.** SiRFP, the α subunit (PDB 6EFV (Tavolieri et al., 2019); 8-mer is octamerization domain; L is flexible linker; Fld is flavodoxin-like domain; FNR/cxn are ferredoxin-NADP$^+$ reductase and connection domains). **b.** SiRHP, the β subunit (PDB 1AOP (Crane et al., 1995); SiRFP-ixn is the N-terminal SiRFP-interaction domain). This color scheme for SiRFP domains and SiRHP are used throughout the manuscript. **c.** Redundancy in possible electron transfer pathways include intra- versus intermolecular transfer within SiRFP (orange arrows) and *cis* versus *trans* electron transfer between SiRFP and SiRHP (yellow arrows). Bold letters show the domain nomenclature while non-bold letters label the cofactors. Tightly-bound SiRFP/SiRHP dimers are outlined in the same way, either black, gray, or none. **d.** Domain composition of SiRFP and SiRHP, colored as in **a.** and **b.**

polypeptide that dimerizes, this conformational change allows the reductase from one subunit to interact with the heme-binding oxidase domain from the partner (Campbell et al., 2014; Haque et al., 2018). The absence of any identified structure of the bound SiR subunits leaves a gap in our understanding of how intersubunit interactions and domain motions govern electron transfer in SiR.

Another aspect of SiR that sets it apart from analogous systems is the way in which SiRFP and SiRHP interact, through interactions between SiRHP's N-terminus and a position on SiRFP's FNR domain that is far from the Fld domain (Askenasy et al., 2018, 2015). This interaction is counterintuitive because the Fld domain must interact with SiRHP to pass electrons to its siroheme-Fe_4S_4 cofactors that funnel the electrons to the siroheme-bound substrate. Nevertheless, a separate, transient interaction between SiRFP's Fld domain and a tightly-bound SiRHP is sufficient for SiR activity because a heterodimeric complex between a monomeric form of SiRFP and full-length SiRHP is active for SO_3^{2-} reduction, albeit at reduced efficiency (Gruez et al., 2000; Zeghouf et al., 2000). SiR's capability for electron transfer is further affected if the flexible linker mediating domain movements of SiRFP is truncated, reducing activity in the heterodimer but not the dodecamer (Tavolieri et al., 2019). These results suggest a model in which the dodecamer transfers electrons through multiple pathways, first from an NADPH to the FAD and on to the FMN cofactor, either within a single SiRFP (intramolecular transfer) or from the FAD of one subunit to the FMN of an adjacent molecule (intermolecular transfer), and then either to a tightly bound SiRHP (in *cis*, Fig. 1c) or to a SiRHP on an adjacent SiRFP subunit (in *trans*, Fig. 1c). This redundancy in electron donor/acceptor pairing could explain SiR's ability to catalyze high-volume electron transfer without releasing partially-reduced intermediates (Hsieh et al., 2010; Lancaster, 2018; Mirts et al., 2018; Oliveira et al., 2011).

In this study, we used small-angle neutron scattering (SANS), selective deuteration, solvent contrast variation, anaerobic reductions, and analytical ultracentrifugation (AUC) to probe the effects of altering the redox state and subunit binding on heterodimers of a monomeric SiRFP and its SiRHP partner. AUC on SiR heterodimers revealed sedimentation coefficients consistent with their respective oligomeric states as *in vitro* reconstituted specimen. SANS was used to measure hydrodynamic parameters and uncover the first-ever solution structures of these heterodimers. Through the use of selective deuteration and neutron contrast variation, the isolated scattering components of SiR heterodimers illuminated the contributions from each subunit to their complexes, informing our understanding of this multisubunit enzyme. Anaerobically reduced SiRFP variants were similarly measured by SANS and showed movements between the Fld and FNR domains. Together, these observations help explain the nature of its complex assembly as well as its capacity for electron transfer.

2. Results

2.1. In vitro reconstitution of SiR complexes and their analysis by AUC

SiR subunits bind one another through interactions between SiRFP's FNR domain and SiRHP's N-terminus (Askenasy et al., 2018, 2015) but the structure of the resulting complex is unknown. The monomeric SiRFP variants used in this study include one in which the 52 N-terminal amino acids are removed to prevent it from octamerization, retaining the Fld and FNR/connection domains but resulting in a 60 kDa monomer (SiRFP-60, Fig. 1d) (Zeghouf et al., 2000). Additional internal truncation of the linker between the Fld and FNR domains is required to immobilize the monomer for structure determination (Tavolieri et al., 2019), SiRFP-60-Δ. An additional variant consists solely of its C-terminal, 43 kDa FNR/connection domains (SiRFP-43, Fig. 1d) (Covès et al., 1999; Zeghouf et al., 2000), representing a minimal, inactive version of SiRFP. Full-length SiRHP was used in all studies because when its N-terminus is removed it can no longer bind SiRFP (Askenasy et al., 2015); however, those amino acids are not present in the X-ray crystal structure (Fig. 1b and d) (Crane et al., 1995).

SiRFP/SiRHP complexes were formed by 1:1 *in vitro* reconstitution. Each subunit and their resulting heterodimers were subjected to sedimentation velocity AUC to confirm that the subunits assembled free of residual monomer (Fig. 2). Each sample exhibited sedimentation coefficient (S) envelopes with single peaks proportional to their molecular weight. The lowest molecular weight fragment of the series, SiRFP-43, sedimented with 3.2 S. SiRFP-60 sedimented at 3.9 S and the 64 kDa SiRHP sedimented at 4.7 S. Additionally, SiRFP-43/SiRHP and SiRFP-60/SiRHP sedimented at 5.5 S and 6.1 S, respectively, and both heterodimers showed distributions with clearly defined, single peaks. These envelopes are consistent with monodisperse specimen suitable for solution scattering experiments, a prerequisite for accurately interpreting scattering data.

2.2. Solution structures of SiR heterodimers

Although structures of the monomeric SiR subunits are known from X-ray crystallography (Crane et al., 1995; Gruez et al., 2000; Tavolieri et al., 2019), no structures exist for higher-order complexes. Consequently, we do not know how the subunits interact such that there is a tight-binding, structural interface independent of the transient, functional interface that mediates electron transfer (Askenasy et al., 2018, 2015). Additionally, we do not know if subunit assembly affects the

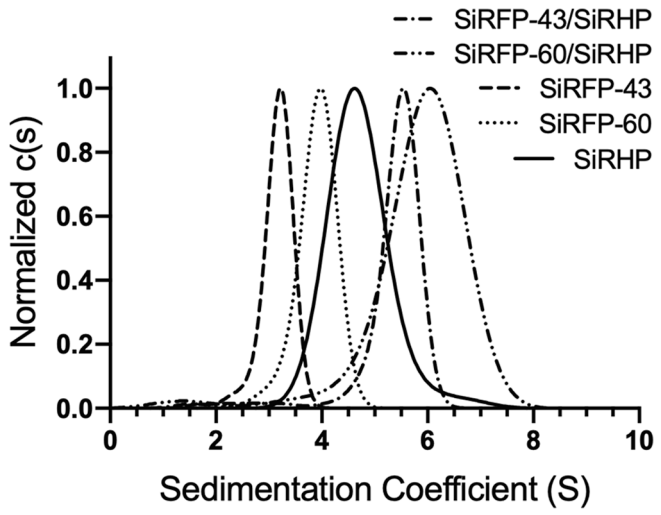

Fig. 2. SiR heterodimers are monodisperse in solution. Sedimentation velocity AUC on SiR monomers (SiRFP-43, SiRFP-60, and SiRHP) and heterodimers (SiRFP-43/SiRHP and SiRFP-60/SiRHP) show sedimentation coefficient envelopes are dominated by single peaks, indicative of monodisperse specimen.

relative domain orientations of the conformationally dynamic SiRFP. We therefore measured neutron scattering of 1:1 SiR heterodimers.

Guinier analysis of the minimal SiRFP-43/SiRHP heterodimer's scattering showed a radius of gyration, R_g, of 32.3 Å and a maximum linear distance, D_{max}, of 99 Å (Fig. 3a, S1a, and Table 1). The bimodal distance distribution function, *P(r)*, of SiRFP-43/SiRHP is consistent with a multi-domain complex, as expected (Fig. 3b). *Ab initio* modeling produced an envelope function that reflects this feature with a real space correlation coefficient (RSC) of 0.86 to an estimated 38 Å resolution with good convergence of the χ^2, R_g, and support volume (Fig. 3c, S2a, and Table S1). The theoretical scattering curve calculated from the envelope matches the experimental data with low residuals (Fig. S2a). The curved shape of one domain was consistent with the dimensions of SiRFP-43, whereas the globular shape of the other domain was consistent with the dimensions of SiRHP, so we placed atomic models accordingly (Fig. 3c). Maps calculated from the atomic models and filtered to 20 Å-resolution fit with a correlation coefficient (CC) of 0.71, calculated in ChimeraX (Table S1) (Goddard et al., 2018). Further, the theoretical scattering curve calculated from the docked X-ray crystal structures of the individual subunits is consistent with the experimental scattering (Fig. S3a). To test our assignment of the curved FNR domain, we also measured the scattering of SiRFP-43, which yielded an R_g of 24.7 Å and D_{max} of 83 Å (Table 1), and whose envelope revealed the expected curve shape, consistent with SiRFP's FNR/connection domains (Fig. S4a).

Guinier analysis of the larger SiRFP-60/SiRHP heterodimer's scattering showed an R_g of 38.0 Å and a D_{max} of 134 Å (Fig. 3a, S1b, and Table 1). Compared to the *P(r)* calculated from the scattering curve for the SiRFP-43/SiRHP dimer, the *P(r)* calculated from the scattering curve for SiRFP-60/SiRHP shows a pronounced bimodal distribution that gradually tails off, suggesting an elongated structure with greater delineation of the domains than in the SiRFP-43/SiRHP dimer (Fig. 3b). *Ab initio* modeling produced a multi-lobed structure with a central curved domain adjacent to a globular domain of similar shape and size to the SiRFP-43/SiRHP dimer (Fig. 3c and d). An additional domain with the same dimensions as SiRFP's N-terminal Fld domain appeared, opposed to the globular domain. The modeled envelope function matches the experimental data well (RSC = 0.89, resolution = 38 Å), with good convergence statistics (Fig. S2b and Table S1). The theoretical scattering curve calculated from the envelope matches the experimental data with low residuals (Fig. S2b). Further, docking the X-ray crystal structure of SiRFP-60-Δ into the envelope shows that SiRFP-60's FNR/connection domains fit well into the central curved domain but with a mismatch in the position of the Fld domain that was resolved by a rigid body motion, whereas SiRHP fit into the globular domain as in the SiRFP-43/SiRHP dimer (CC = 0.76, Fig. 3d and Table S1). The theoretical scattering curve calculated from the docked X-ray crystal structures of SiRFP-60/SiRHP is consistent with its experimental scattering curve (Fig. S3b). We also collected neutron scattering on the dimer formed by assembling SiRFP-60-Δ with SiRHP (SiRFP-60-Δ/SiRHP) as a control to determine if the full-length linker was too flexible to accurately model. The R_g, D_{max}, and envelope were nearly identical to those determined for SiRFP-60/SiRHP (Table 1 and Fig. S4b).

2.3. Flexibility in SiRFP

The degree of compaction and unfolding within a protein can be qualitatively assessed by Kratky plot analysis performed on small-angle scattering data (Putnam et al., 2007; Rambo and Tainer, 2011). Kratky plots of primarily globular, compact proteins exhibit bell-shaped peaks at low q values, whereas plots of multidomain proteins containing flexible linkers show an asymmetric bell-shaped peak at low q with a plateau that decays at higher q. A compact protein containing a disordered extension will additionally exhibit a continuous rise at high q values. A dimensionless Kratky plot normalized by forward scattering ($I(0)$) and R_g of SiRFP-43 and SiRFP-60 indicates that the former is compact whereas the latter exhibits additional flexibility (Fig. S5a). The extreme flexibility of the linker that joins SiRFP-60's Fld and FNR domains, which is 30 amino acids long out of a 599, is predicted to have characteristics associated with intrinsic disorder (Askenasy et al., 2018). Without truncating SiRFP-60's linker, the Fld domain is not sufficiently ordered to contribute to the X-ray crystal structure (Gruez et al., 2000; Tavolieri et al., 2019).

2.4. Isolated SiRFP-60 scattering within the heterodimer

To confirm our domain assignment in the SiRFP-60/SiRHP heterodimer, we isolated the scattering contribution of each subunit by selectively deuterating SiRHP (D-SiRHP), experimentally-determining its contrast match point (CMP) (Fig. S6), and altering the solvent contrast to match either subunit. The subunit that was matched-out by manipulating the H_2O:D_2O solvent ratio will be demarked by an asterisk throughout. SANS measurements on SiRFP-60/D-SiRHP* in buffer at D-SiRHP's CMP isolated the scattering from SiRFP-60 in the context of its heterodimer structure (Fig. 4a). The R_g and D_{max} of SiRFP-60/D-SiRHP* is larger than the reported values for monomeric SiRFP-60, previously measured by SANS (Tavolieri et al., 2019). Specifically, the R_g increased from 32.2 to 33.1 Å and its D_{max} increased from 113 to 124 Å (Table 1 and Fig. S1c and d). This manifests in a *P(r)* plot for SiRFP-60/D-SiRHP* whose distribution function decays like an extended molecule, which is reflected in its *ab initio* model (RSC = 0.88, resolution = 31 Å) with good convergence (Fig. 4b, c, S2c, and Table S1). The extended, multi-lobed shape agrees with our assignment of SiRFP-60's position in the heterodimer, including the Fld domain repositioned from its place in the X-ray structure of SiRFP-60-Δ and solution structure of SiRFP-60 (CC = 0.71 for both models, Fig. 4c, d, and Table S1) (Tavolieri et al., 2019). Theoretical scattering curves calculated from the envelope function as well as the docked atomic models correlate with the experimental data with low residuals (Figs. S2c and S3c). Kratky plot analysis shows that the overall flexibility of SiRFP-60 remained constant upon heterodimer formation with SiRHP (Fig. S5b).

As a control, we also measured the scattering of SiRFP-43/D-SiRHP*, which revealed only subtle changes to the R_g/D_{max} and the envelope of SiRHP-bound SiRFP-43 compared to its monomeric form, as expected due to the absence of the Fld domain in SiRFP-43 (Fig. S4c and Table 1). In addition, scattering of SiRFP-60-Δ /D-SiRHP* agreed with SiRFP-60/D-SiRHP*, further supporting our interpretation of the Fld domain motion upon SiRHP binding (Fig. S4d and Table 1).

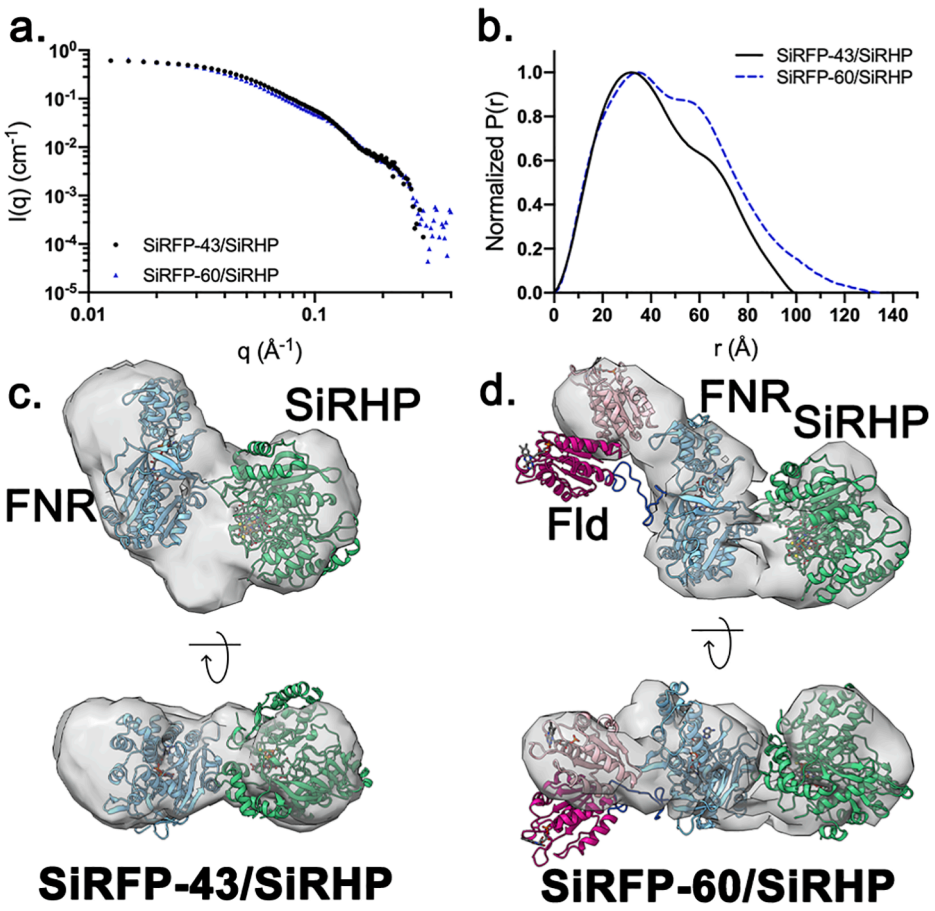

Fig. 3. Solution structures of heterodimeric SiR: SiRFP-43/SiRHP and SiRFP-60/SiRHP. **a.** Scattering profiles of SiRFP-43/SiRHP and SiRFP-60/SiRHP show gradual decay into higher *q* regions. **b.** Distance distribution functions for heterodimers' scattering in **a.** show multicomponent systems. The *ab initio* models (grey density) of SiRFP-43/SiRHP (**c.**) and SiRFP-60/SiRHP (**d.**) with high-resolution structures superimposed ((**c.**) SiRFP-43, PDB 1DDG (Gruez et al., 2000) and (**d.**) SiRFP-60-Δ, PDB 6EFV (Tavolieri et al., 2019)). High-resolution structures are colored as in Fig. 1. In **d.**, the rearranged Fld domain is colored light pink.

2.5. SiRHP undergoes compaction upon binding SiRFP-60

We next measured the contribution of D-SiRHP to the scattering of the SiRFP-60/D-SiRHP heterodimer by preparing SiRFP-60/D-SiRHP in buffer at SiRFP-60's CMP (Fig. 5a). Compared to the scattering of monomeric D-SiRHP, SiRFP-60*/D-SiRHP exhibited a decrease in its R_g from 25.9 to 24.1 Å (Table 1, Fig. S1e and S1f). D_{max} values obtained from *P(r)* analyses of D-SiRHP and SiRFP-60*/D-SiRHP reflected this compaction, from 75 to 66 Å, respectively (Fig. 5b and Table 1). Solution structures of SiRFP-60*/D-SiRHP and D-SiRHP obtained from *ab initio* modeling also manifest these differences with a rearrangement of density in the models between the monomer and heterodimer (RSC = 0.95 and 0.86 to estimated resolutions of 19.8 and 32.7 Å, respectively; Fig. 5c, d, and Table S1). Theoretical scattering curves calculated from the *ab initio* models of SiRFP-60*/D-SiRHP and D-SiRHP both correspond to their respective experimental scattering curves with low residuals, as does the theoretical scattering curve calculated from the atomic model of SiRHP (Figs. S2d, e, S3d, and e) (Crane et al., 1995). The atomic model of SiRHP fits into the volumes representing SiRFP-60*/D-SiRHP or D-SiRHP with a CC of 0.71 or 0.89, respectively (Table S1). As controls, we measured D-SiRHP's contribution to the scattering of the other heterodimer variants (SiRFP-60-Δ */D-SiRHP and SiRFP-43*/D-SiRHP), which also showed contraction of D-SiRHP in both the hydrodynamic parameters and modeled envelopes (Fig. S4e and f, Table 1).

Previously performed intrinsic disorder prediction and protease protection assays further suggest that the N-terminus of SiRHP is not ordered when it is free from SiRFP, in part explaining why it must be removed for crystallization (Askenasy et al., 2018; Crane et al., 1995). In contrast, the ferredoxin-dependent SiRHP homologs from *Zea mays* and *Mycobacterium tuberculosis* have structured N-termini (Kim et al., 2016; Schnell et al., 2005). To test our interpretation that the missing amino acids contribute to SiRHP's scattering (79 amino acids out of 570 total), we modeled the space they might occupy by superimposing those X-ray crystal structures (PDB 5H8V and 1ZJ8). The calculated theoretical scattering curve fits to the experimental scattering of heterodimeric SiRFP-60*/D-SiRHP (Fig. S7a) with a χ^2 of 2.9 whereas the fit for monomeric D-SiRHP yielded a χ^2 of 9.8 (Fig. S7b). This agrees with Kratky plot analyses that show a decrease in disorder in SiRFP-60*/D-SiRHP's relative to D-SiRHP, demonstrated by the plot's less pronounced rise at high *q* (Fig. S5c).

2.6. SiRFP-60's Fld domain further repositions upon dithionite reduction

By analogy with homologous enzymes like CPR and NOS (Campbell et al., 2014; Huang et al., 2013), we predicted that SiRFP-60 exhibits redox-dependent domain movements that allow reducing equivalents to pass from the NADPH-reduced FAD to the FMN cofactor. In CPR, the domains open relative to one another upon FMN reduction to allow transfer of reducing equivalents to the heme-containing oxidase. Unlike CPR, however, SiRFP-60 adopts an extended state in solution when it is oxidized (Fig. 4a, b, and d) (Huang et al., 2013; Tavolieri et al., 2019). Therefore, to test the effect of redox state on SiRFP's structure, SiRFP-60 was reduced with 10 M equivalents (Eq) of sodium dithionite in an anaerobic glovebox before being transferred to a cuvette sealed from atmosphere and measured with SANS. Upon titrating dithionite, 10 Eq was found to fully reduce the enzyme based on its UV–visible spectrum (Fig. S8).

The scattering of reduced SiRFP-60 revealed an open conformation (Fig. 6a), even more exaggerated than its oxidized conformation (Tavolieri et al., 2019). Compared to the previously reported solution structure of oxidized SiRFP-60 (Fig. 4d), 10 Eq-reduced SiRFP-60's R_g

Table 1
Hydrodynamic parameters of sulfite reductase.

Sample	D_2O (%)	Domain/protein composition	Mass (kDa)	Oligomeric state	R_g (Å)	D_{max} (Å)
SiRFP-43/SiRHP	90	FNR/SiRHP	107	Dimer (αβ)	32.3 ± 0.1	99
SiRFP-43	90	FNR	43	Monomer (α)	24.7 ± 0.3	83
SiRFP-60/SiRHP	90	Fld-linker-FNR/SiRHP	124	Dimer (αβ)	38.0 ± 0.2	134
SiRFP-60-Δ/SiRHP	90	Fld-ΔAAPSQS-FNR/SiRHP	123	Dimer (αβ)	37.8 ± 0.3	132
SiRFP-60/D-SiRHP*	86	Fld-linker-FNR/D-SiRHP	124	Dimer (αβ)	33.1 ± 0.5	124
SiRFP-60	90	Fld-linker-FNR	60	Monomer (α)	32.2 ± 0.1	113
SiRFP-43/D-SiRHP*	86	FNR/D-SiRHP	107	Dimer (αβ)	25.2 ± 0.7	73
SiRFP-60-Δ/D-SiRHP*	86	Fld-ΔAAPSQS-FNR/D-SiRHP	123	Dimer (αβ)	33.5 ± 0.8	123
SiRFP-60*/D-SiRHP	41	Fld-linker-FNR/D-SiRHP	124	Dimer (αβ)	24.1 ± 0.6	66
D-SiRHP	41	D-SiRHP	64	Monomer (β)	25.9 ± 0.3	75
SiRFP-43*/D-SiRHP	41	FNR/D-SiRHP	107	Dimer (αβ)	23.7 ± 0.8	65
SiRFP-60-Δ*/D-SiRHP	41	Fld-ΔAAPSQS-FNR/D-SiRHP	123	Dimer (αβ)	23.6 ± 0.9	68
SiRFP-60 Reduced	90	Fld-linker-FNR	60	Monomer (α)	33.8 ± 0.4	122
SiRFP-60-Δ Reduced	90	Fld-ΔAAPSQS-FNR	59	Monomer (α)	33.2 ± 0.3	114

* Matched-out component

increases from 32.2 to 33.8 Å and the D_{max} shifts from 113 to 122 Å (Fig. 6b, S1g, and Table 1) whereas the envelope of reduced SiRFP-60 (RSC = 0.88, resolution = 28.1 Å, Table S1) shows its characteristic bent FNR domain and the globular Fld domain in a novel conformation (Fig. 6c). The theoretical scattering curve calculated from the *ab initio* model corresponds to its experimental scattering curve with low residuals and the model resulting from the repositioned Fld domain fits the experimental scattering well (CC = 0.80, Figs. S2f, S3f, and Table S1). We also measured the scattering of dithionite-reduced SiRFP-60-Δ, which similarly showed extension compared to its oxidized state, albeit not as dramatic as in SiRFP-60 (Fig. S4g and Table 1) (Tavolieri et al., 2019). Note, this experiment cannot be performed on the heterodimers because oxidized dithionite is a substrate for SiRHP, so the system would be in multiple redox states as it consumes the dithionite (Siegel et al., 1974).

3. Discussion

3.1. SANS is the ideal technique to study the solution scattering of SiR

Here, we present a systematic analysis of dimeric SiR variants' neutron scattering, allowing us to calculate the first solution structures of this essential metabolic oxidoreductase. By using SANS rather than small-angle X-ray scattering (SAXS), we were able to assess the contribution of each subunit to the scattering through contrast manipulation. Alteration of the H_2O:D_2O ratio of the buffers allowed us to isolate the scattering of SiRFP or SiRHP within the dimer. SANS is unique in allowing this type of contrast matching measurement, as is the fact that neutrons are less destructive than X-rays and therefore do not artificially impact the redox state of the system (Ankner et al., 2013). The series of structures show how SiR's reductase and oxidase subunits interact and how the positioning of SiRFP's Fld domain is impacted by both SiRHP binding and its redox environment.

The 8:4 stoichiometry of reductase to oxidase subunits in SiR has been long-hypothesized as important in its high-volume electron transfer chemistry by increasing the local concentration of reduced Fld domains for each SiRHP active site (Askenasy et al., 2018; Siegel and Davis, 1974; Tavolieri et al., 2019). This hypothesis predicts that SiRHP can recruit a transiently-interacting Fld domain from either a tightly-bound subunit (*cis* electron transfer) or an adjacent partner (*trans* electron transfer) (Fig. 1c). SiR uses three NADPH molecules as reducing equivalents for each molecule of S^{2-} it generates, so access to more than one Fld domain would enhance the probability of a productive interaction with SiRHP. The changes that we see to the scattering envelopes from our SANS measurements on SiR dimer variants show for the first time how this might happen through motion of SiRFP's Fld domain in response to both its oligomeric and redox states.

3.2. SiRHP binding alters SiRFP-60's interdomain orientation

When SiRFP is oxidized, it is in an open conformation where the small Fld domain is extended away from the curved FNR domain, connected by a 30 amino acid long linker (Fig. 4d) (Tavolieri et al., 2019). Upon SiRHP binding, the Fld domain rotates by about 30° relative to its position in the unbound form (Fig. 3d), a conformational change that we confirmed with contrast matching experiments to isolate SiRFP-60's contribution to the dimer's scattering (Fig. 4c). The resolution of the envelope is not sufficient to explain the mechanism by which SiRHP binding far from the Fld domain affects its conformation, but we are missing a very important detail about SiRHP: the structure of its N-terminus. As we have docked the atomic models, the N-terminal most amino acid in SiRHP's structure (L81) is about 60 Å away from the last amino acid in SiRFP's linker (P236). This distance could certainly be spanned by those N-terminal amino acids absent from current high-resolution structures (Crane et al., 1995) to affect the conformation of the linker and determine the position of the Fld domain relative to the FNR domain to which SiRHP binds.

3.3. SiRHP undergoes compaction upon binding SiRFP-60

We also used SANS and contrast matching to reveal how SiRFP-60 binding affects the shape of SiRHP. SiRHP's D_{max} decreases by almost 10 Å upon binding its partner, which can be visualized in the envelope function as a transition to a more globular shape. This compaction is likely the result of a rearrangement at its N-terminus, which is not resolved in the crystal structure, but known to be required for SiRFP binding (Askenasy et al., 2018; Crane et al., 1995). We propose that binding to SiRFP's FNR domain either induces the flexible N-terminus to contract as it mediates intersubunit contacts or binds SiRFP as an extended peptide that would not contribute strongly to SiRHP's scattering. That SiRHP binding affects SiRFP's domain structure suggests that the latter may be occurring but the former cannot be excluded.

3.4. SiRFP reduction repositions the Fld domain

In our model for the positions of SiRFP-60 and SiRHP within the envelopes modeled from neutron scattering, SiRHP is far from the Fld domain that would be responsible for funneling electrons to it within this minimal dimer (Fig. 3d). This placement is consistent with the results from contrast matching experiments (Figs. 4 and 5) as well as previously-reported mutational analysis that identified amino acids in the FNR domain of SiRFP as important for SiRHP binding (Askenasy et al., 2018, 2015). Nevertheless, *cis* electron transfer to a tightly-bound SiRHP in the minimal dimeric complex occurs, albeit at a rate of ~50% that of the holoenzyme (Tavolieri et al., 2019; Zeghouf et al., 2000). Our SANS analysis reveals a dramatic reorientation of the Fld domain upon

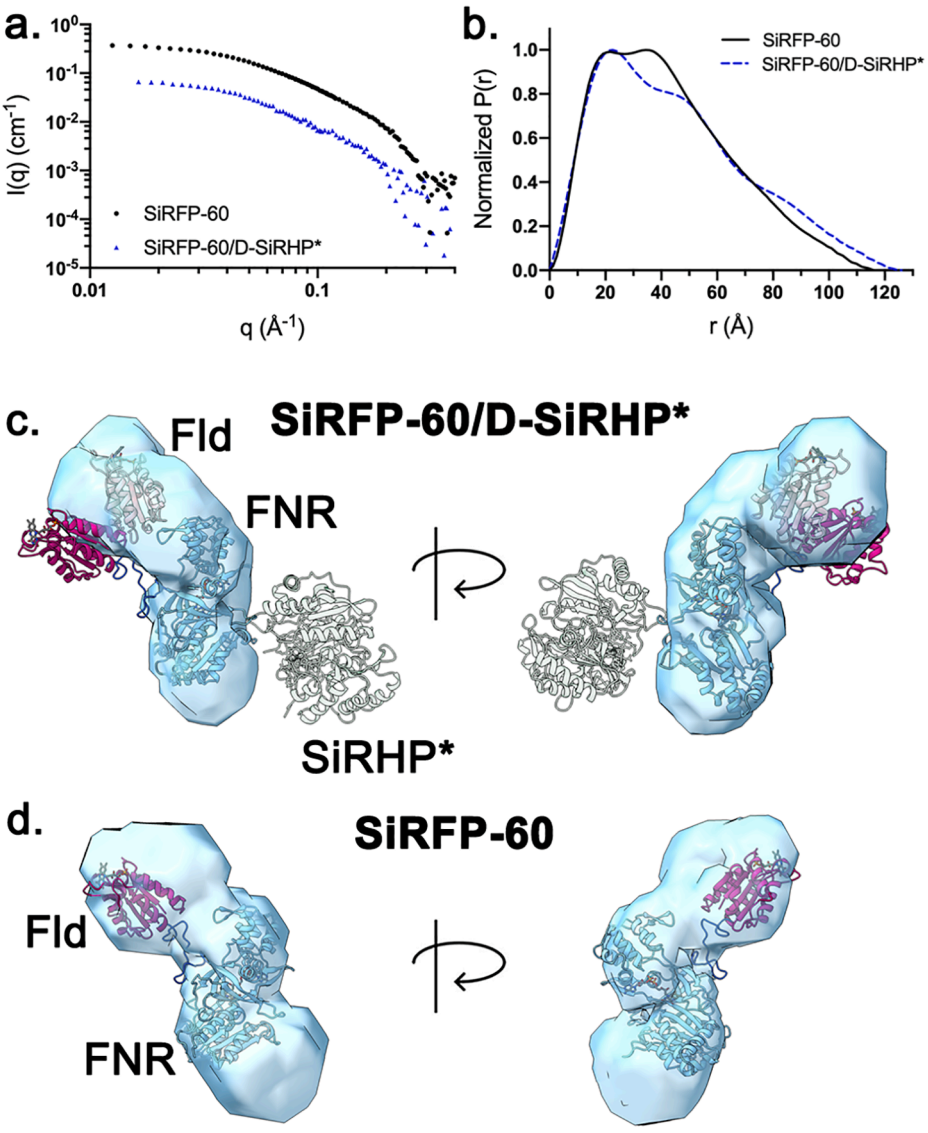

Fig. 4. SiRFP-60 exhibits an extended conformation upon binding SiRHP. **a.** Scattering profile of SiRFP-60/D-SiRHP* and SiRFP-60. **b**. The distance distribution plot of SiRFP-60/D-SiRHP* exhibits a shift in its bilobed peaks relative to the previously reported, oxidized form (Tavolieri et al., 2019). **c.** Model (blue density) of SiRFP-60/D-SiRHP* with SiRFP-60-Δ's crystal structure superimposed, colored as in Fig. 1. Matched-out D-SiRHP is shown transparently and the rearranged Fld domain is colored light pink. **d.** SiRFP-60's solution structure, as previously reported (Tavolieri et al., 2019).

SiRFP-60 reduction (Fig. 6).

4. Conclusions

4.1. Possible SiRFP conformations for cis or trans electron transfer

The envelope functions of SiR heterodimers determined from SANS provide the first solution structures depicting how SiRHP binds SiRFP's FNR domain, far from the Fld domain from which the electrons move from the reductase to the oxidase. We confirmed our domain assignments by measuring scattering of SiR dimers containing a SiRFP variant that lacks the Fld domain as well as with the use of contrast variation to isolate each dimer component. Analyzing the hydrodynamic parameters and resulting envelope functions allowed us to make three observations that further our understanding of how subunit assembly and redox state affect SiR's structure, with possible implications for how the domains move for electron transfer. First, surprisingly, subunit binding impacts the position of the Fld domain even though it is far from where SiRHP binds, suggesting a mechanism by which *trans* electron transfer might take place in the context of the dodecameric holoenzyme because SiRHP binding positions the Fld domain away from it, perhaps pointing to an adjacent subunit (Fig. 7a). Second, SANS of monomeric D-SiRHP and SiRFP/D-SiRHP heterodimers suggest SiRHP's N-terminus undergoes a structural rearrangement upon complex assembly (Fig. 7b). Third, superimposition of the bi-lobed feature of the reduced SiRFP-60 onto the envelope of the whole heterodimer shows that reduction swivels SiRFP-60's Fld domain towards the binding position of SiRHP, suggesting a mechanism for *cis* electron transfer to a tightly-bound oxidase partner (Fig. 7c). Together, these observations show that SiRFP's interaction with SiRHP and redox state position SiRFP's Fld domain for high-volume electron transfer between subunits.

5. Materials and methods

5.1. Expression, purification, and characterization of SiR proteins

Hydrogenated SiRFP and SiRHP proteins were expressed and purified as previously described (Askenasy et al., 2018, 2015; Tavolieri et al., 2019). Briefly, pBAD vectors (Thermo Fisher Scientific, Waltham, MA, USA) containing the genes encoding either N-terminally truncated/*hexa*-histidine tagged SiRFP or untagged SiRHP from *Escherichia coli* (*E. coli*) were transformed into *E. coli* LMG194 cells (Invitrogen, Carlsbad, CA, USA) for recombinant protein expression. Proteins were purified to homogeneity with the use of nickel affinity, anion exchange, and size exclusion chromatography.

SiR heterodimers were formed by mixing purified monomeric SiRFP

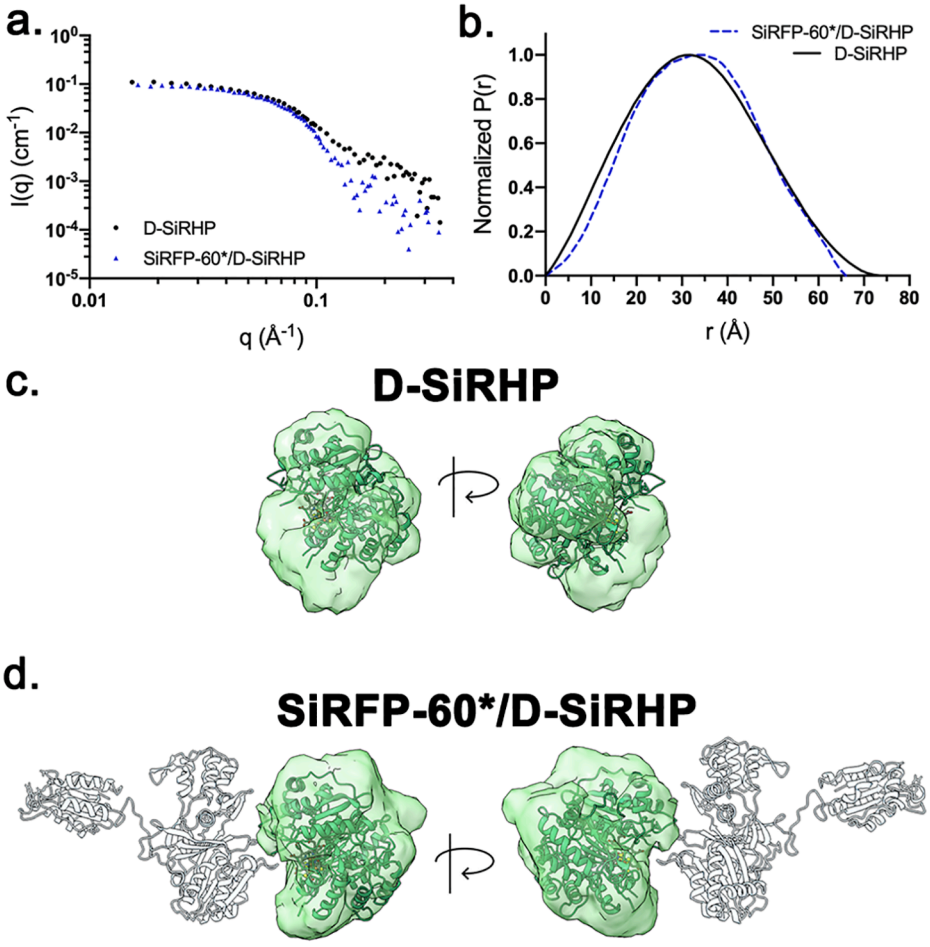

Fig. 5. SiRHP undergoes compaction upon binding SiRFP. **a.** Scattering profiles of D-SiRHP and SiRFP-60*/D-SiRHP. **b.** Distance distribution plots for the scattering profiles in **a.** show D-SiRHP adopts a reduced D_{max} upon binding SiRFP-60. Models (green density) of D-SiRHP (**c.**) and SiRFP-60*/D-SiRHP (**d.**). SiRHP's crystal structure is superimposed on both models and SiRFP-60 is shown transparently to reflect its matching-out in **d**.

and SiRHP subunits followed by incubation for 30 min on ice. They were then loaded onto a 5 mL HisTrap FF nickel affinity chromatography column (Cytiva, Marlborough, MA, USA) that had been previously equilibrated with SPG buffer (17 mM succinic acid, 574 mM sodium dihydrogen phosphate, pH 6.8, 374 mM glycine, 200 mM NaCl) and eluted with a gradient of the same buffer containing 500 mM imidazole. Fractions obtained during the imidazole gradient were analyzed via SDS-PAGE and fractions containing heterodimer were loaded onto a Superose 6 10/300 size exclusion chromatography column (Cytiva, Marlborough, MA, USA) equilibrated with SANS buffer (50 mM KPi, pH 7.8, 100 mM NaCl, 1 mM EDTA) to separate residual monomers from the heterodimers.

Expression of D-SiRHP was carried out with fed-batch cultivation at Oak Ridge National Laboratory's Bio-Deuteration Laboratory (ORNL, Oak Ridge, TN, USA). *E. coli* BL21 (DE3) cells (New England Biolabs, Ipswich, MA, USA) were transformed with the untagged SiRHP-expressing pBAD vector (Askenasy et al., 2015). Transformants were adapted to D_2O by transferring an inoculum from Enfors minimal medium prepared with H_2O and 100 μg/mL carbenicillin into the same medium with increasing D_2O content (0, 50, and 70%) (Törnkvist et al., 1996). Once cells were growing in 70% D_2O medium, a 250 mL preculture was used to inoculate 3.75 L of 70% D_2O Enfors minimal media in a BioFlo 310 bioreactor (Eppendorf, Hauppauge, NY, USA). Cells were grown at 37 °C with dry, sterile air flow and agitation varying between 200 and 600 rpm to maintain dissolved oxygen above 30% saturation. 10% (w/v) NaOH in 70% D_2O was fed on demand to maintain a pD > 7.3. Addition of feed solution consisting of 10% (w/v) H-glycerol, 0.2% $MgSO_4$, and 100 μg/mL carbenicillin in 70% D_2O was initiated when the dissolved oxygen spiked upon depletion of H-glycerol from the batch medium. Fourteen hours post-inoculation and at an OD_{600} of 10, the temperature set point was reduced to 25 °C and D-SiRHP expression was induced by the addition of 0.05% L-arabinose in 70% D_2O. 12 h post-induction, cells were harvested by centrifugation at 6,000 × g for 40 min and resuspended in lysis buffer (65 mM KPi, pH 7.8, 200 mM NaCl, 1 mM EDTA) before being flash-frozen with liquid nitrogen (LN_2).

D-SiRHP was purified as previously described for SiRHP with minor adjustments for scaling the amount of cell mass used during initial lysis and purification steps. Cell mass was thawed and diluted to 10% (w/v) with lysis buffer supplemented with 100 μg/mL PMSF and 1 μg/mL Pepstatin A. Cells were lysed at 15,000 psi in three passages through a water-cooled EmulsiFlex-C3 homogenizer (Avestin, Ottawa, ON, CA) and lysate collected in a beaker on ice. 0.1% (v/v) polyethyleneimine was added to the lysate while stirring for 30 min at 6 °C. Lysate was clarified by centrifugation at 13,000 × g for 25 min. Two successive ammonium sulfate cuts (31.5% and 52.5% (w/v)) were performed on the supernatant. The first precipitate was discarded after centrifugation at 13,000 × g for 25 min and the second was resuspended in lysis buffer. The resuspension was passed over a Sephadex G-25 desalting column and subsequently dialyzed into 5 mM KPi, pH 7.8, 1 mM EDTA solution overnight at 6 °C. The resulting solution was spun at 10,000 × g for 10 min before loading the supernatant onto a DEAE Sepharose Fast Flow anion exchange chromatography column (Cytiva, Marlborough, MA, USA) equilibrated with fresh dialysis buffer before being eluted with a gradient of 50 mM KPi, pH 7.8, 1 mM EDTA. Fractions containing D-

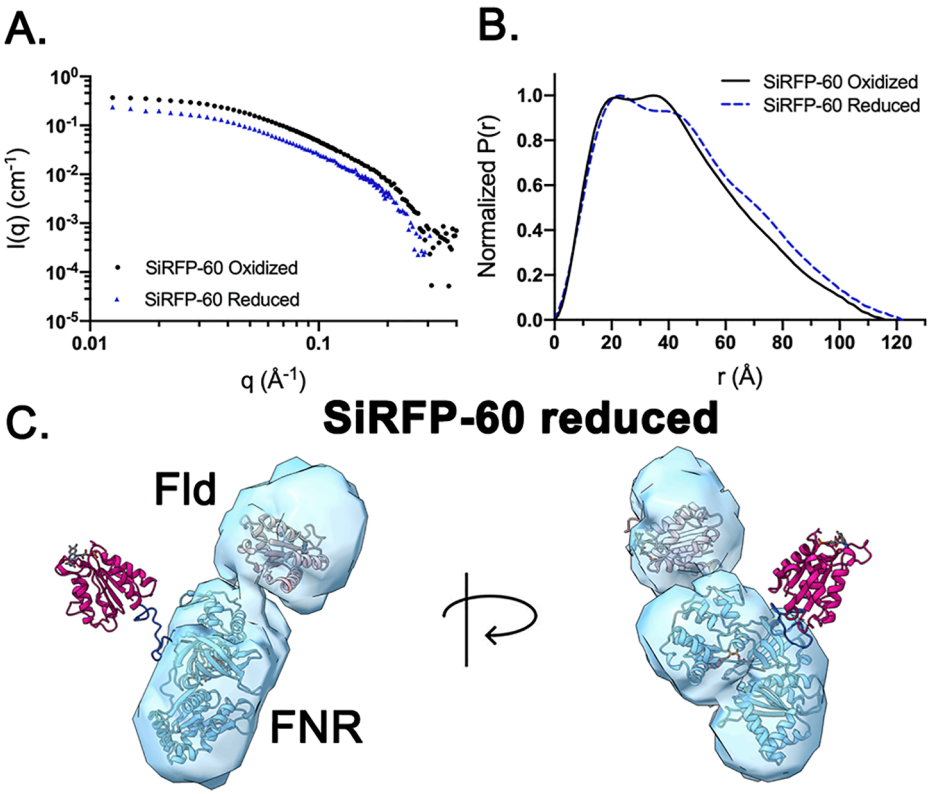

Fig. 6. SiRFP-60 exhibits an extended conformation upon reduction. **a.** Scattering profile of oxidized (Tavolieri et al., 2019) and reduced SiRFP-60. **b.** The distance distribution plot of reduced SiRFP-60 shows an extended state and a shift in its bilobed peaks relative to the previously reported, oxidized form (Tavolieri et al., 2019). **c.** Model of reduced SiRFP-60 (blue) with the repositioned Fld domain from the crystal structure of SiRFP-60-Δ (light pink). (See Fig. 4**d** for oxidized SiRFP-60).

SiRHP were concentrated with a 10 kDa MWCO polyethersulfone membrane-containing centrifugal concentrator and then loaded onto a Sephacryl S-300 HR size exclusion chromatography column (Cytiva, Marlborough, MA, USA) previously equilibrated with SANS buffer. The purified fractions were pooled and concentrated as before and then flash frozen with LN_2. Partially deuterated SiR heterodimers were assembled in the same manner as their hydrogenated counterparts.

D-SiRHP was evaluated using SAXS to assess deuterated sample quality in varying amounts of D_2O on a BioSAXS-2000 system (Rigaku Americas, TX, USA). SAXS was measured on D-SiRHP in SANS buffer composed of either 0, 75, or 100% D_2O. D-SiRHP's scattering overlapped with that of hydrogenated SiRHP (H-SiRHP) under identical conditions and was free from aggregation (Fig. S6a and b).

5.2. Analytical ultracentrifugation

Sedimentation velocity experiments were performed using a ProteomeLab XL-1 analytical ultracentrifuge with the use of an AN60-Ti rotor and Epon-2 channel centerpieces (Beckman Coulter, Brea, CA, USA). Protein samples were diluted with SANS buffer to concentrations yielding an absorbance of 0.5 at 280 nm as measured with an 8454 UV–Vis spectrophotometer (Agilent Technologies, Santa Clara, CA, USA). Samples were then loaded into cell assemblies with sapphire windows for collecting absorbance data. Rotor speeds of 40,000 or 32,500 rpm were used for monomeric and heterodimeric SiR samples, respectively. All samples were run at 20 °C for 7 h. Scan data were imported into UltraScan III software, after which 2-D spectrum and enhanced van Holde-Weischet analyses were completed to fit time-invariant noise and obtain sedimentation coefficient values, respectively (Demeler and van Holde, 2004; Demeler and Scott, 2005). Sedimentation coefficients were corrected for the density and viscosity of SANS buffer at 20 °C.

5.3. Anaerobic reductions

SiRFP variants were reduced with sodium dithionite in an anaerobic glove box using SANS buffer prepared with 90% D_2O that had been degassed using freeze–pumpthaw cycling and inert gas substitution. 10 Eq of sodium dithionite were added to the sample and allowed to incubate for 30 min. Dithionite was chosen as reducing agent in place of the cellular electron donor, NADPH, because it independently reduces the flavins without binding to the protein, thus resulting in a homogenous population of molecules. That is, a mixed state of NADPH/$NADP^+$-bound molecules would not contribute to the scattering. The effect of the reduction was monitored with UV–visible spectroscopy on an 8453 model spectrophotometer (Agilent Technologies, Santa Clara, CA, USA). In preparation for SANS measurements, 320 μL of reduced protein solution was loaded into 1 mm pathlength circular-shaped quartz cuvettes (Hellma USA, Plainville, NY, USA) and sealed with vacuum grease, rubber septa, and parafilm.

5.4. SANS data collection

SANS data were collected on the Extended Q-Range Small-Angle Neutron Scattering Diffractometer (EQ-SANS, Beam Line 6) at the Spallation Neutron Source (SNS) located at ORNL. Two configurations were used in 60 Hz operation mode: 4 m sample-to-detector distance with 2.5–6.1 Å wavelength band and 1.3 m sample-to-detector distance with 4.0–8.3 Å wavelength band (Zhao et al., 2010) to obtain the relevant wavevector transfer, $Q = 4\pi \sin(\theta)/\lambda$, where 2θ is the scattering angle and λ is the neutron wavelength. Samples were loaded into 1 mm pathlength circular quartz cuvettes and data collected at 8 °C with the simultaneous introduction of dry air to prevent condensation on cuvettes. Scattering data were circularly averaged and reduced to one-dimensional scattering profiles using MantidPlot (Arnold et al., 2014). The measured scattering intensity was corrected for detector sensitivity and scattering contributions from buffers and empty cell, and then placed on absolute scale using a calibrated porasilica standard (Wignell

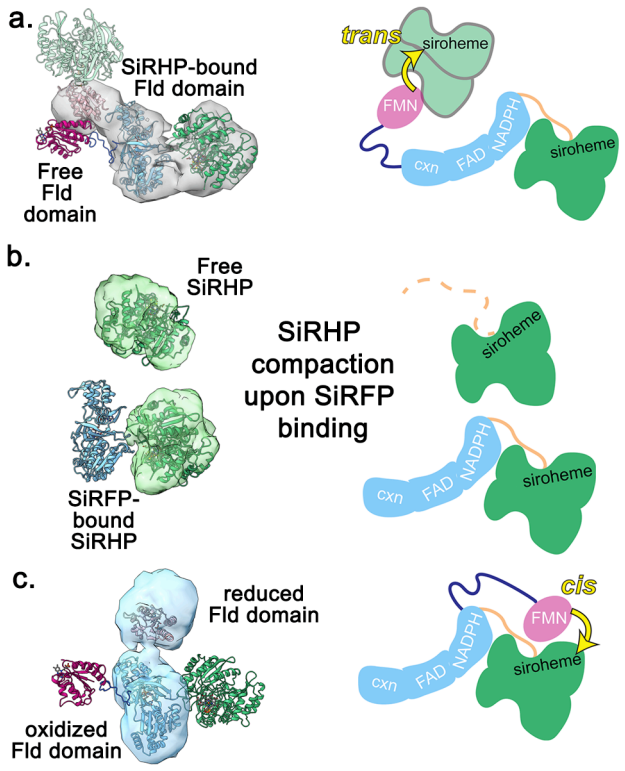

Fig. 7. Model for SiRFP-SiRHP interactions. **a.** In the SiRFP-60/SiRHP dimer (gray density), SiRFP's Fld domain (light pink) opens away from its FNR domain (light blue), perhaps positioning it for electron transfer to a SiRHP (transparent green) that is tightly-bound to an adjacent subunit. **b.** SiRHP (green density) becomes compact upon binding SiRFP's FNR domain (light blue), likely from reorganization of its N-terminus. **c.** In reduced SiRFP-60, the Fld domain (light pink) is repositioned to orient towards SiRHP (green), suggesting a mechanism for electron transfer in *cis*, *i.e.,* from SiRFP (light blue density) to a tightly-bound SiRHP (green).

and Bates, 1987). Replicate measurements were summed and those from each instrument configuration were merged. Incoherent background subtractions were also implemented in MantidPlot before the datasets were exported for analysis.

Hydrogenated samples were dialyzed into SANS buffer prepared with 90% D_2O prior to SANS measurements to obtain sufficient contrast. Partially deuterated samples were dialyzed into mixtures containing 41 or 86% D_2O to contrast match either the hydrogenated SiRFP or D-SiRHP of the heterodimer complexes, respectively. 41% D_2O was chosen as the CMP for SiRFP from theoretical calculations based on amino acid sequence and agreement with CMPs of other hydrogenated proteins (Whitten 2008). The CMP of D-SiRHP (86% D_2O) was determined experimentally by performing a contrast series of SANS measurements at 0, 41, 55, 75, 85, and 100% D_2O, determining the $I(0)$ of each measurement, and then plotting a linear fit of $\sqrt{I(0)}$ vs. % D_2O (Fig. S6c and d). A CMP of 86% D_2O was to be expected given the results of studies following similar deuteration protocols (Dunne et al., 2017; Leiting et al., 1998; White et al., 2019). The contrast tool of MULCh was used to check the amount of deuteration by using the experimentally determined CMP as input, which gave a deuteration level of 54% and is in agreement with our expression conditions (Whitten 2008).

For SANS measurements on reduced proteins, the anaerobicity of the samples were monitored over the course of data collection for changes in their scattering curves, indicative of changes due to re-oxidation. Comparisons of initial and final scattering curves showed no changes and the summed measurements were taken for analysis.

5.5. SANS data analysis and modeling

After reduction in MantidPlot, data were imported into the ATSAS 3.0.1 suite (European Molecular Biology Laboratory, Hamburg Outstation), managed in PRIMUS (Konarev et al., 2003; Petoukhov et al., 2012). R_g and $I(0)$ were determined in PRIMUS, whereas D_{max} and $P(r)$ analyses were calculated in GNOM (Svergun, 1992). R_g and $I(0)$ were obtained using a Guinier approximation (a linear fit of a $\ln[I(q)]$ vs. q^2 plot, where $R_g \times q_{max} < 1.3$) (Guinier and Fournet, 1955). D_{max} values were obtained through an indirect Fourier transform of the scattering data, yielding real-space distance distribution functions for each specimen, with D_{max} determined by where the function decays to $r = 0$. The $P(r)$ data were used as inputs for *ab initio* modeling using DENSS (DENsity from Solution Scattering) software to create density maps that were then refined to produce the final scattering envelopes (Grant, 2018). Dimensionless Kratky plots were generated in BioXTAS RAW (Hopkins et al., 2017). Comparisons of SANS data to theoretical scattering curves were calculated in CRYSON (Svergun et al., 1998) with D_2O fraction in the solvent specified to mimic the experimental contrast conditions. High-resolution structures obtained from the Protein Data Bank (PDB) were positioned into solution structures in UCSF ChimeraX (Berman et al., 2000; Goddard et al., 2018). All SANS models were submitted to the Small Angle Scattering Biological Data Bank (SASBDB) with the following accession codes: SASDKH6 (SiRFP-43/SiRHP); SASDKJ6 (SiRFP-60/SiRHP); SASDKK6 (D-SiRHP); SASDKL6 (reduced SiRFP-60); SASDKM6 (SiRFP-60*/D-SiRHP); and SASDKN6 (SiRFP-60/D-SiRHP*) (Kikhney et al., 2020).

Author contributions

D.T.M., C.B.S., G.N., and M.E.S. performed SANS experiments and analyzed data. D.T.M. performed wet lab experiments and analyzed data. D.T.M. and M.E.S. designed wet lab experiments. D.T.M and K.L. W. designed and performed deuteration experiments. M.E.S. designed the project and wrote the manuscript together with D.T.M. All authors reviewed, approved, and contributed to the final version of the manuscript.

Declaration of Competing Interest

The authors declare that they have no known competing financial interests or personal relationships that could have appeared to influence the work reported in this paper.

Acknowledgements

We thank Claudius Mundoma for helpful conversations regarding the analysis of AUC data, Christopher Stroupe and Tristan Dilbeck for careful reading of the manuscript. A portion of this research at ORNL's Spallation Neutron Source was sponsored by the Scientific User Facilities Division, Office of Basic Energy Sciences, U.S. Department of Energy. The Office of Biological and Environmental Research also supported work at the Oak Ridge National Laboratory Center for Structural Molecular Biology. This work was supported by National Science Foundation grants MCB1856502 and CHE1904612 to M.E.S.

Appendix A. Supplementary data

Supplementary data to this article can be found online at https://doi.org/10.1016/j.jsb.2021.107724.

References

Ankner, J.F., Heller, W.T., Herwig, K.W., Meilleur, F., Myles, D.A., 2013. Neutron scattering techniques and applications in structural biology. Curr. Protoc. Protein Sci. Chapter 17 (Unit17), 16.

Arnold, O., Bilheux, J.C., JBorreguero, J.M., Buts, A., Campbell, S.I., Chapon, L., Doucet, M., Draper, N., Ferraz Leal, R., Gigg, M.A., Lynch, V.E., Markvardsen, A., Mikkelson, D.J., Mikkelson, R.L., Miller, R., Palmen, K., Parker, P., Passos, G., Perring, T.G., Peterson, P.F., Ren, R., Reuter, M.A., Savici, A.T., Taylor, J.W., Taylor, R.J., Tolchenov, R., Zhou, W., Zikovsky, J., 2014. Mantid – data analysis and visualization package for neutron scattering and μ SR experiments. Nucl. Instrum. Methods Phys. Res. Sect. A 764, 156–166.

Askenasy, I., Pennington, J.M., Tao, Y., Marshall, A.G., Young, N.L., Shang, W., Stroupe, M.E., 2015. The N-terminal domain of Escherichia coli assimilatory NADPH-sulfite reductase hemoprotein is an oligomerization domain that mediates holoenzyme assembly. J. Biol. Chem. 290, 19319–19333.

Askenasy, I., Murray, D.T., Andrews, R.M., Uversky, V.N., He, H., Stroupe, M.E., 2018. Structure-function relationships in the oligomeric NADPH-dependent assimilatory sulfite reductase. Biochemistry 57, 3764–3772.

Berman, H.M., Westbrook, J., Feng, Z., Gilliland, G., Bhat, T.N., Weissig, H., Shindyalov, I.N., Bourne, P.E., 2000. The protein data bank. Nucl. Acids Res. 28, 235–242.

Campbell, M.G., Smith, B.C., Potter, C.S., Carragher, B., Marletta, M.A., 2014. Molecular architecture of mammalian nitric oxide synthases. Proc. Natl. Acad. Sci. U.S.A. 111, E3614–3623.

Covès, J., Lebrun, C., Gervasi, G., Dalbon, P., Fontecave, M., 1999. Overexpression of the FAD-binding domain of the sulphite reductase flavoprotein component from Escherichia coli and its inhibition by iodonium diphenyl chloride. Biochem. J. 342 (Pt 2), 465–472.

Crane, B., Siegel, L., Getzoff, E., 1995. Sulfite reductase structure at 1.6 angstrom - evolution and catalysis for reduction of inorganic anions. Science 270, 59–67.

Demeler, B., Scott, D., 2005. UltraScan – a Comprehensive Data Analysis Software Package for Analytical Ultracentrifugation Experiments. Analytical Ultracentrifugation: Techniques and Methods, 210–230.

Demeler, B., van Holde, K., 2004. Sedimentation velocity analysis of highly heterogeneous systems. Anal. Biochem. 335, 279–288.

Dunne, O., Weidenhaupt, M., Callow, P., Martel, A., Moulin, M., Perkins, S.J., Haertlein, M., Forsyth, V.T., 2017. Matchout deuterium labelling of proteins for small-angle neutron scattering studies using prokaryotic and eukaryotic expression systems and high cell-density cultures. Eur. Biophys. J. 46, 425–432.

Freeman, S.L., Martel, A., Raven, E.L., Roberts, G.C.K., 2017. Orchestrated domain movement in catalysis by cytochrome P450 Reductase. Sci. Rep. 7, 9741.

Freeman, S.L., Martel, A., Devos, J.M., Basran, J., Raven, E.L., Roberts, G.C.K., 2018. Solution structure of the cytochrome P450 reductase-cytochrome. J. Biol. Chem. 293, 5210–5219.

Goddard, T.D., Huang, C.C., Meng, E.C., Pettersen, E.F., Couch, G.S., Morris, J.H., Ferrin, T.E., 2018. UCSF ChimeraX: Meeting modern challenges in visualization and analysis. Protein Sci. 27, 14–25.

Grant, T., 2018. Ab initio electron density determination directly from solution scattering data vol. 15, 191–193.

Gruez, A., Pignol, D., Zeghouf, M., Covès, J., Fontecave, M., Ferrer, J.L., Fontecilla-Camps, J.C., 2000. Four crystal structures of the 60 kDa flavoprotein monomer of the sulfite reductase indicate a disordered flavodoxin-like module. J. Mol. Biol. 299, 199–212.

Guinier, A., Fournet, G., 1955. Small Angle Scattering of X-rays. Wiley, New York.

Hamdane, D., Xia, C., Im, S.C., Zhang, H., Kim, J.J., Waskell, L., 2009. Structure and function of an NADPH-cytochrome P450 oxidoreductase in an open conformation capable of reducing cytochrome P450. J. Biol. Chem. 284, 11374–11384.

Haque, M.M., Tejero, J., Bayachou, M., Kenney, C.T., Stuehr, D.J., 2018. A cross-domain charge interaction governs the activity of NO synthase. J. Biol. Chem. 293, 4545–4554.

Hopkins, J.B., Gillilan, R.E., Skou, S., 2017. BioXTAS RAW: improvements to a free open-source program for small-angle X-ray scattering data reduction and analysis. J. Appl. Crystallogr. 50, 1545–1553.

Hsieh, Y.C., Liu, M.Y., Wang, V.C., Chiang, Y.L., Liu, E.H., Wu, W.G., Chan, S.I., Chen, C. J., 2010. Structural insights into the enzyme catalysis from comparison of three forms of dissimilatory sulphite reductase from Desulfovibrio gigas. Mol. Microbiol. 78, 1101–1116.

Huang, W.C., Ellis, J., Moody, P.C., Raven, E.L., Roberts, G.C., 2013. Redox-linked domain movements in the catalytic cycle of cytochrome p450 reductase. Structure 21, 1581–1589.

Im, S.C., Waskell, L., 2011. The interaction of microsomal cytochrome P450 2B4 with its redox partners, cytochrome P450 reductase and cytochrome b(5). Arch. Biochem. Biophys. 507, 144–153.

Iyanagi, T., Xia, C., Kim, J.J., 2012. NADPH-cytochrome P450 oxidoreductase: prototypic member of the diflavin reductase family. Arch. Biochem. Biophys. 528, 72–89.

Kikhney, A.G., Borges, C.R., Molodenskiy, D.S., Jeffries, C.M., Svergun, D.I., 2020. SASBDB: towards an automatically curated and validated repository for biological scattering data. Protein Sci. 29, 66–75.

Kim, J., Nakayama, M., Toyota, H., Kurisu, G., Hase, T., 2016. Structural and mutational studies of an electron transfer complex of maize sulfite reductase and ferredoxin. J. Biochem. 160, 101–109.

Konarev, P.V., Volkov, V.V., Sokolova, A.V., Koch, M.H.J., Svergun, D.I., 2003. PRIMUS: a windows PC-based system for small-angle scattering data analysis. J. Appl. Cryst. 36, 1277–1282.

Lancaster, K.M., 2018. Revving up an artificial metalloenzyme. Science 361, 1071–1072.

Leiting, B., Marsilio, F., O'Connell, J.F., 1998. Predictable deuteration of recombinant proteins expressed in Escherichia coli. Anal. Biochem. 265, 351–355.

Mirts, E.N., Petrik, I.D., Hosseinzadeh, P., Nilges, M.J., Lu, Y., 2018. A designed heme-[4Fe-4S] metalloenzyme catalyzes sulfite reduction like the native enzyme. Science 361, 1098–1101.

Murphy, M.J., Siegel, L.M., Kamin, H., Rosenthal, D., 1973. Reduced nicotinamide adenine dinucleotide phosphate-sulfite reductase of enterobacteria. II. Identification of a new class of heme prosthetic group: an iron-tetrahydroporphyrin (isobacteriochlorin type) with eight carboxylic acid groups. J. Biol. Chem. 248, 2801–2814.

Oliveira, T.F., Franklin, E., Afonso, J.P., Khan, A.R., Oldham, N.J., Pereira, I.A., Archer, M., 2011. Structural insights into dissimilatory sulfite reductases: structure of desulforubidin from desulfomicrobium norvegicum. Front. Microbiol. 2, 71.

Olteanu, H., Banerjee, R., 2001. Human methionine synthase reductase, a soluble P-450 reductase-like dual flavoprotein, is sufficient for NADPH-dependent methionine synthase activation. J. Biol. Chem. 276, 35558–35563.

Petoukhov, M.V., Franke, D., Shkumatov, A.V., Tria, G., Kikhney, A.G., Gajda, M., Gorba, C., Mertens, H.D., Konarev, P.V., Svergun, D.I., 2012. New developments in the program package for small-angle scattering data analysis. J. Appl. Crystallogr. 45, 342–350.

Putnam, C.D., Hammel, M., Hura, G.L., Tainer, J.A., 2007. X-ray solution scattering (SAXS) combined with crystallography and computation: defining accurate macromolecular structures, conformations and assemblies in solution. Q. Rev. Biophys. 40, 191–285.

Rambo, R.P., Tainer, J.A., 2011. Characterizing flexible and intrinsically unstructured biological macromolecules by SAS using the Porod-Debye law. Biopolymers 95, 559–571.

Schnell, R., Sandalova, T., Hellman, U., Lindqvist, Y., Schneider, G., 2005. Siroheme- and [Fe-4-S-4]-dependent NirA from Mycobacterium tuberculosis is a sulfite reductase with a covalent Cys-Tyr bond in the active site. J. Biol. Chem. 280, 27319–27328.

Siegel, L.M., Murphy, M.J., Kamin, H., 1973. Reduced nicotinamide adenine dinucleotide phosphate-sulfite reductase of enterobacteria. I. The Escherichia coli hemoflavoprotein: molecular parameters and prosthetic groups. J. Biol. Chem. 248, 251–264.

Siegel, L.M., Davis, P.S., Kamin, H., 1974. Reduced nicotinamide adenine dinucleotide phosphate-sulfite reductase of enterobacteria. 3. The Escherichia coli hemoflavoprotein: catalytic parameters and the sequence of electron flow. J. Biol. Chem. 249, 1572–1586.

Siegel, L.M., Davis, P.S., 1974. Reduced nicotinamide adenine dinucleotide phosphate-sulfite reductase of enterobacteria. IV. The Escherichia coli hemoflavoprotein: subunit structure and dissociation into hemoprotein and flavoprotein components. J. Biol. Chem. 249, 1587–1598.

Svergun, D.I., 1992. Determination of the regularization parameter in indirect-transform methods using perceptual criteria. J. Appl. Crystallogr. 25, 495–503.

Svergun, D.I., Richard, S., Koch, M.H., Sayers, Z., Kuprin, S., Zaccai, G., 1998. Protein hydration in solution: experimental observation by x-ray and neutron scattering. Proc. Natl. Acad. Sci. U.S.A. 95, 2267–2272.

Tavolieri, A.M., Murray, D.T., Askenasy, I., Pennington, J.M., McGarry, L., Stanley, C.B., Stroupe, M.E., 2019. NADPH-dependent sulfite reductase flavoprotein adopts an extended conformation unique to this diflavin reductase. J. Struct. Biol. 205, 170–179.

Törnkvist, M., Larsson, G., Enfors, S., 1996. Protein release and foaming in Escherichia coli cultures grown in minimal medium vol. 15, 231–237.

Wang, M., Roberts, D.L., Paschke, R., Shea, T.M., Masters, B.S., Kim, J.J., 1997. Three-dimensional structure of NADPH-cytochrome P450 reductase: prototype for FMN- and FAD-containing enzymes. Proc. Natl. Acad. Sci. U.S.A. 94, 8411–8416.

White, M.R., Mitrea, D.M., Zhang, P., Stanley, C.B., Cassidy, D.E., Nourse, A., Phillips, A. H., Tolbert, M., Taylor, J.P., Kriwacki, R.W., 2019. C9orf72 poly(PR) dipeptide repeats disturb biomolecular phase separation and disrupt nucleolar function. Mol. Cell 74, 713–728.e716.

Whitten, A.E., S.C.a.J.T., 2008. MULCh: modules for the analysis of small-angle neutron contrast variation data from biomolecular assemblies. J. Appl. Cryst. 41, 222–226.

Wignell, G.D., Bates, F.S., 1987. Absolute calibration of small-angle neutron scattering data. J. Appl. Crystallogr. 20, 28–40.

Xia, C., Panda, S.P., Marohnic, C.C., Martásek, P., Masters, B.S., Kim, J.J., 2011a. Structural basis for human NADPH-cytochrome P450 oxidoreductase deficiency. Proc. Natl. Acad. Sci. U.S.A. 108, 13486–13491.

Xia, C., Hamdane, D., Shen, A.L., Choi, V., Kasper, C.B., Pearl, N.M., Zhang, H., Im, S.C., Waskell, L., Kim, J.J., 2011b. Conformational changes of NADPH-cytochrome P450 oxidoreductase are essential for catalysis and cofactor binding. J. Biol. Chem. 286, 16246–16260.

Zeghouf, M., Fontecave, M., Coves, J., 2000. A simplifed functional version of the Escherichia coli sulfite reductase. J. Biol. Chem. 275, 37651–37656.

Zhang, H., Yokom, A.L., Cheng, S., Su, M., Hollenberg, P.F., Southworth, D.R., Osawa, Y., 2018. The full-length cytochrome P450 enzyme CYP102A1 dimerizes at its reductase domains and has flexible heme domains for efficient catalysis. J. Biol. Chem. 293, 7727–7736.

Zhao, J.K., Gao, C.Y., Liu, D., 2010. The extended Q-range small-angle neutron scattering diffractometer at the SNS. J. Appl. Crystallogr. 43, 1068–1077.